# Trailing edge serrations

## Effect of their flap angle on flow and acoustics

Arce Leon, Carlos; Merino Martinez, Roberto; Ragni, Daniele; Pröbsting, Stefan; Avallone, Francesco; Singh, A.; Madsen, Jesper

**Publication date**
2017

**Document Version**
Submitted manuscript

**Published in**
7th International Conference on Wind Turbine Noise

7th International Conference
on
Wind Turbine Noise
Rotterdam – 2nd to 5th May 2017

# Trailing Edge Serrations — Effect of Their Flap Angle on Flow and Acoustics

**Carlos Arce León, LM Wind Power, the Netherlands: caar@lmwindpower.com**
**Roberto Merino-Martínez, TU Delft, the Netherlands: r.merinomartinez@tudelft.nl**
**Daniele Ragni, TU Delft, the Netherlands: d.ragni@tudelft.nl**
**Stefan Pröbsting, TU Delft, the Netherlands: s.probsting@tudelft.nl**
**Francesco Avallone, TU Delft, the Netherlands: f.avallone@tudelft.nl**
**Ashish Singh, LM Wind Power, India: asi@lmwindpower.com**
**Jesper Madsen, LM Wind Power, Denmark: jema@lmwindpower.com**

## Summary
Trailing edge serrations have been proven to work as a passive noise reduction device. Nevertheless, they have also previously been found to increase noise in a particular frequency range, argued in earlier research to be due to the misalignment of the serrations with the direction of the flow in the wake. It emerges as a high-frequency noise increase in a broadband region of the spectrum. This study investigates the effect of serration-flow misalignment on the noise emissions using acoustic beamforming, and finds a correlation with observations made on the flow using particle image velocimetry (PIV). The hydrodynamic source of the noise increase is hereby identified, and a Strouhal number relation for the high-frequency noise increase is proposed.

## 1. Introduction
Trailing edge serrations have become the prevailing device for turbulent boundary layer-trailing edge noise (TBL-TE noise) reduction on wind turbine blades (Hurault et al., 2015; Mathew et al., 2016; Oerlemans, 2016). Their performance nevertheless depends on their correct design and installation. Tooth length and width recommendations with respect to the local airfoil boundary layer thickness, $\delta$, have been proposed by Gruber, Joseph, and Chong, 2011. It is furthermore widely accepted that their edge should be thin with respect to $\delta$ to avoid the introduction of additional noise mechanisms, such as vortex shedding[1]. But until recently (Arce León et al., 2016b; Arce León et al., 2016c; Vathylakis et al., 2016), the effect of their flap angle has not been thoroughly addressed.

This parameter is nevertheless greatly important in the application of trailing edge

[1] A similar but distinct device, the trailing edge serrations of cutout type, follows a different design approach, and to avoid tonal noise issues caused by the thick trailing edge, the application of meshes has been proposed by Vathylakis, Chong, and Joseph, 2015.

serrations as a high-volume product in the wind turbine industry. Many careful considerations in their design must be made (Mathew et al., 2016), and the flap angle, $\varphi$, is one of them. One needs to contemplate its placement on the blade, and a set of its operating conditions (twist, the range of pitch, and the local inflow velocities, for example). It needs to adapt to the local airfoil shape and the way it will be attached. One should consider and ease the procedural implications of its installation, something that is not easy, especially if it is to be done by a technician dangling from a rope. These considerations should be made such that they minimize the risk of serration-flow misalignment—that is, how much the serrations are misaligned with respect to the direction that the flow in the wake would have if the serrations were not present.

Other than for aerodynamic reasons (minimizing the serration impact on the airfoil performance, unless that is desired), there is good aeroacoustic sense in pursuing serration-flow alignment. It has been previously hypothesized that serration-flow misalignment is the cause of an observed increase in noise with respect to the straight trailing edge. This phenomenon has been observed in wind tunnel measurements, as in Dassen et al., 1996; Gruber, Joseph, and Chong, 2010; Finez et al., 2011, and also in field measurements of serrated wind turbine blades, for example Oerlemans et al., 2009, and independent measurements by LM Wind Power. The conjecture argues that the high frequency noise originates from the regions between the serration teeth, where the flapwise tooth misalignment with the mean flow increases the turbulence intensity.

The noise increase is known to happen after a certain frequency, $f_c$, entitled as *crossover frequency*. Gruber, Joseph, and Chong, 2010 proposed that it is related to a constant Strouhal number which is based on the boundary layer thickness and the freestream velocity,

$$\mathrm{St}_c = \frac{f_c \delta}{U_\infty}. \tag{1}$$

Using a serrated NACA 6512-10 airfoil and measuring $f_c$ at different freestream velocities, it was established that $\mathrm{St}_c \approx 1$. A variance of around 30% was found, attributed to potential variations in the boundary layer thickness introduced by the serrations. It was further explained by the fact that the boundary layer was not measured for all the given freestream velocities, but was instead approximated using the software XFOIL. A specific relation of $\mathrm{St}_c$ to the airfoil angle of attack, $\alpha$, is not clear from the research, but results for different angles of attack are provided in Gruber, 2012.

The research here presented aims to review the proposed constant Strouhal number approximation by combined acoustic and aerodynamic measurements of a serrated NACA 0018 airfoil with regard to its original straight trailing edge shape. Several freestream velocities are investigated, 30, 35 and 40 m/s, which at the highest yields a Reynolds number of approximately 533,000. Angles of attack of 0°, 6°, 12° (geometric) and serration flap angles of 0° and 6° are prescribed. The boundary layer thicknesses at all the investigated conditions have been measured on both the pressure and suction sides for the straight edge using PIV.

The hydrodynamic source of this high frequency noise increase is further explored by means of high-speed stereoscopic particle image velocimetry (S-PIV). The time-

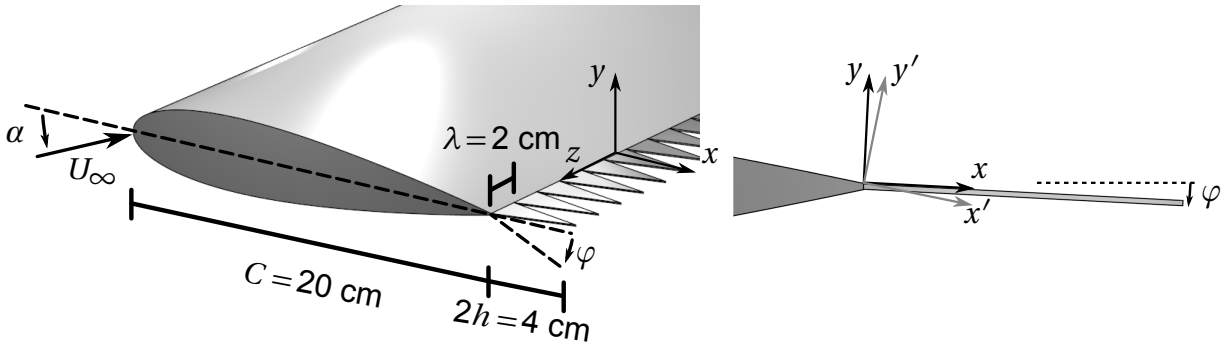


Figure 1: Airfoil and serration dimensions (left), and convention used for the coordinate system rotation over the airfoil and serration surfaces (right).

resolved boundary layer flow is thereby described on both sides, allowing an inspection of mean flow parameters and turbulence characteristics that was previously incomplete. An extended study of the research here presented has been compiled in Arce León et al., 2017.

## 2. Experimental Setup

The experiment was conducted at the vertical wind tunnel facility (V-Tunnel) of the Delft University of Technology. This is a low turbulence tunnel ($< 1\%$ turbulence intensity, Ghaemi, Ragni, and Scarano, 2012) with an open test section. The two side-plates in this setup form a structural support for the airfoil, and help to maintain a quasi-two dimensional flow behavior over the airfoil, offering a relatively low aspect ratio of 2. This setup further allows an acoustic direct line of sight to the airfoil trailing edge. The wind tunnel nozzle has a dimension of $0.4 \times 0.4\,\mathrm{m}^2$.

The airfoil used was a NACA 0018 profile of 0.4 m span and 0.2 m chord. It was machined from aluminium and has a modular trailing edge that allows converting the straight trailing edge into a serrated edge by the insertion of laser-cut serrations of flat-plate type. The latter had a length of $2h = 4$ cm, a width of $\lambda = 2h/2 = 2$ cm, and a constant thickness of 1 mm (the same as the baseline airfoil trailing edge thickness). A schematic of of the serrated airfoil and its dimensions can be seen in figure 1. The coordinate system definition is also shown indicated. For consistency, when boundary layer results are shown, it is rotated about the $z$ axis to keep $y$ wall-normal in accordance with the definition of boundary layer. The prime nomenclature will be omitted later for conciseness.

The boundary layer transition was forced using a narrow (2 cm) tape of three-dimensional roughness elements (carborundum, 0.6 mm nominal size) that spanned the whole airfoil at both the suction and pressure sides. It was placed at 20% chord. By doing this it is ensured that laminar boundary layer instability noise is avoided and only TBL-TE noise is produced. The boundary layer was confirmed to remain turbulent at the trailing edge using a microphone probe.

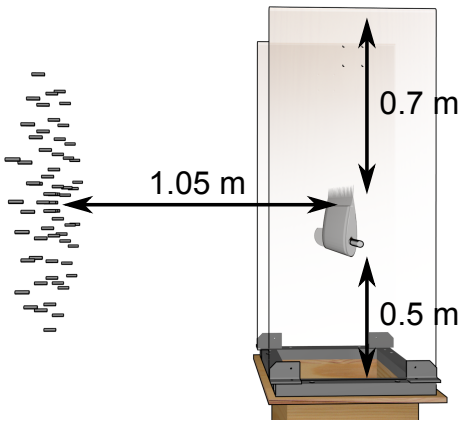


Figure 2: Schematic of the setup used for the acoustic measurements. The side plates are rendered here transparent.

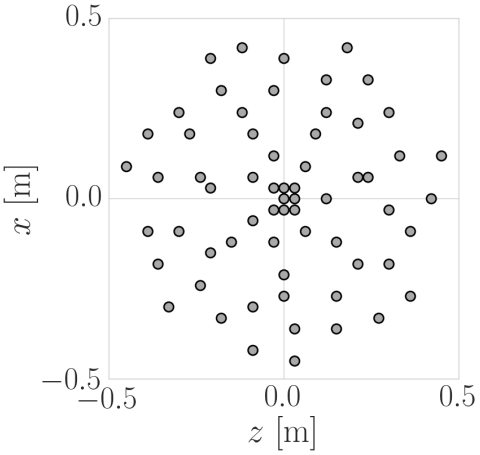


Figure 3: Microphone distribution within the array.

### 2.1 Acoustic measurements

Acoustic phased array measurements were used to acquire the trailing edge noise source emissions at 30, 35 and 40 m/s. This method was preferred as it allows the inspection of only the region of interest, avoiding unwanted noise sources. Examples of the latter are the noise of the tunnel nozzle and the side-plate edges, and that produced by the side-plate boundary layer interaction with the airfoil. The velocities at which the measurements were taken were chosen because they offered a good signal-to-noise ratio (SNR). A schematic of the setup is shown in figure 2.

Recordings were made over 60 s total time with a pistonphone-calibrated multi-arm logarithmic spirally distributed 64 microphone array (figure 3, Mueller, 2002; Pröbsting et al., 2016). A sampling frequency of 50 kHz was used. The data was averaged using time blocks of 2048 samples of 40.96 ms each. These were windowed by a Hanning weighing function with 50% overlap, to which a fast Fourier transform was applied.

Conventional frequency domain beamforming was used (Johnson and Dudgeon, 1993; Sijtsma, 2010), for which a scan grid of potential sources is defined. The grid covered a trailing edge-centered rectangle from $z =$ -0.22 m to 0.22 m in the airfoil spanwise direction, and $z =$ -0.3 m to 0.3 m in its streamwise direction. The results were integrated, using the Source Power Integration method (Sijtsma, 2010), around the trailing edge region, in the area between $z =$ -0.1 m and 0.1 m, and $x =$ -0.06 m and 0.06 m. The beamforming results can be seen in the source maps of figure 4, where the integration region is indicated with a dashed rectangle.

Results will be presented in one-third octave bands between 1 and 5 kHz. Respectively, the limits are established by the effective array aperture (0.9 m) and a sufficiently good SNR (larger than 10 dB).

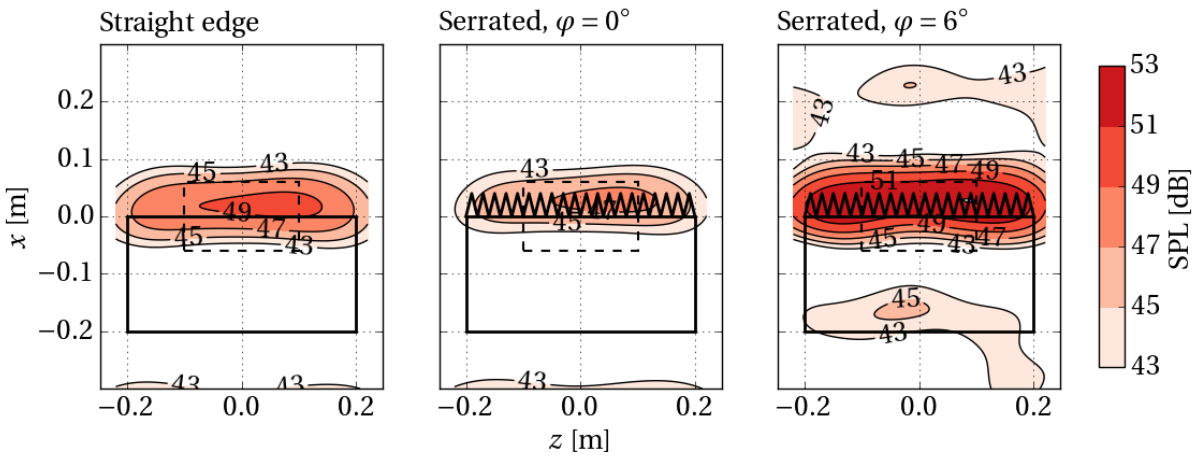


Figure 4: Source map results of the frequency domain beamforming at a one-third octave band of 4 kHz for the straight and serrated trailing edges. The airfoil and serrations are indicated, and the integration region is marked with the dashed rectangle.

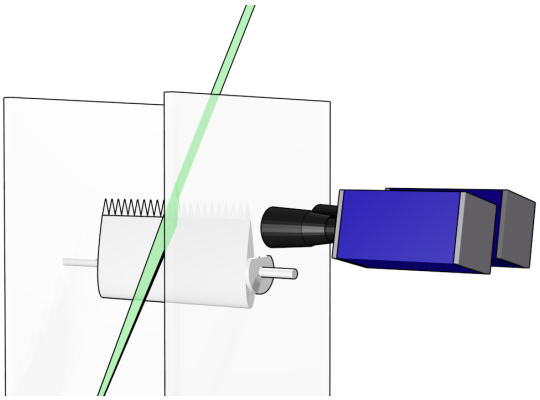

Figure 5: Planar PIV measurement setup.

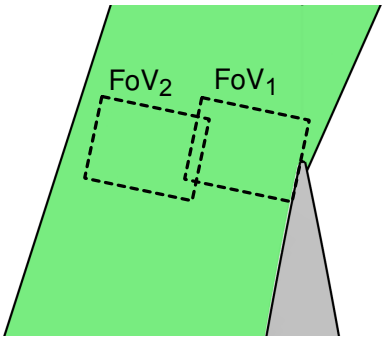


Figure 6: FoV configuration.

## 2.2 Flow measurements

Two sets of PIV measurements were conducted to characterize the flow. The first aimed at obtaining the boundary layer thickness from the airfoil with the straight trailing edge. Boundary layer properties were measured over both the suction and pressure sides with two-component planar particle image velocimetry (2C-PIV) for all the freestream velocities and angles of attack at which acoustic and S-PIV flow measurements were carried out. The second set of measurements were performed with S-PIV and were used to characterize the boundary layer flow statistics, both time-averaged and time-resolved. Both systems are described below.

The 2C-PIV system (schematic in figure 5) used a low-repetition rate configuration. Tracer particles in the flow (SAFEX, mean diameter $\sim 1\,\mu$m) were illuminated with an Nd:YAG 200 mJ/pulse laser (Quantel Twin BSL 200) with an acquisition frequency of 5 Hz. 300 uncorrelated image pairs were obtained with two CCD cameras (PCO Sensicam QE) with their respective field of view (FoV) overlapping, as shown in figure 6. The

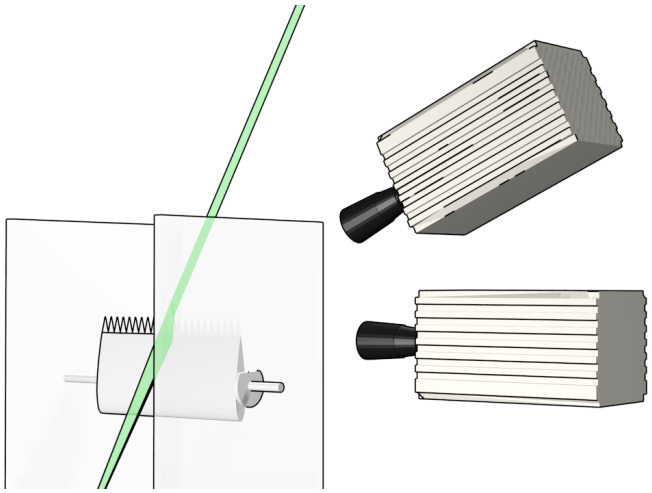

Figure 7: Stereoscopic PIV measurement setup.

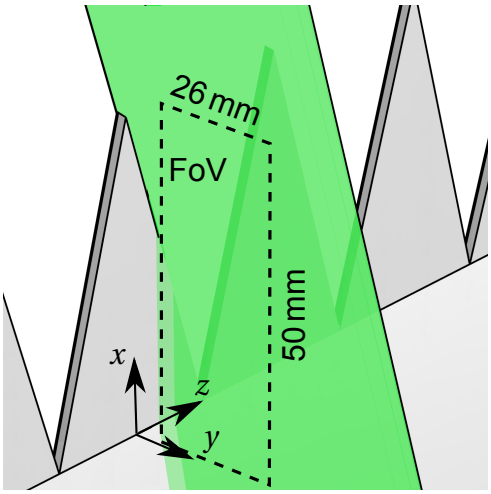


Figure 8: Location of the field of view for the stereoscopic PIV measurements in the $z/\lambda = 0.25$ measurement plane.

combined FoV yielded an effective measurement region of $36 \times 16$ mm. The cameras were arranged as shown in figure 5 with their optical axes perpendicular to the flow direction. They have a sensor size of $1376 \times 1040$ px with a pixel pitch of 6.7 $\mu$m/px, and were equipped with 105 mm focal length Nikon NIKKOR objectives operated at an F-number of $f/8$. The resulting digital image resolution was approximately 65 px/mm. At a pulse separation time of 15 $\mu$s, a freestream particle displacement of about 20 px was obtained for 20 m/s.

The S-PIV system (figure 7) was used in two configurations; one for the acquisition of time-averaged data, and another for time-resolved data. In both cases, the tracer particles (same as in the 2C-PIV system) were illuminated with a dual-cavity Nd:YLF high-speed laser (Quantronix Darwin Duo, $2 \times 25$ mJ/pulse at 500 Hz frequency) capable of $2 \times 25$ mJ/pulse. Two CMOS cameras (Photron Fastcam SA1.1, $1024 \times 1024$ px, 20 $\mu$m/px pixel-pitch, 12 bit resolution) were set up in stereoscopic configuration (35° angle offset between the optical axes) in order to resolve the out-of-plane (spanwise) velocity component $w$. The same camera optics were used as before, with an F-number of $f/5.6$. A digital image resolution of 20 px/mm was obtained over an effective FoV of $26 \times 50$ mm$^2$, as indicated in figure 8 (the sensor was cropped to $512 \times 1024$ px to reach the desired high-frequency acquisition rate).

For the time-averaged measurements, a 250 Hz acquisition frequency was used to acquire 2000 image pairs at a pulse separation of 50 $\mu$s, resulting in a freestream particle displacement of around 12.5 px. The time-resolved flow information was obtained with 10,100 particle images per case at 10 kHz acquisition frequency, such that time separation between image pairs of 100 $\mu$s was achieved, resulting in a freestream particle displacement of around 25 px. Due to technical restrictions imposed by the highest achievable acquisition frequency of the current S-PIV system (10 kHz), the freestream

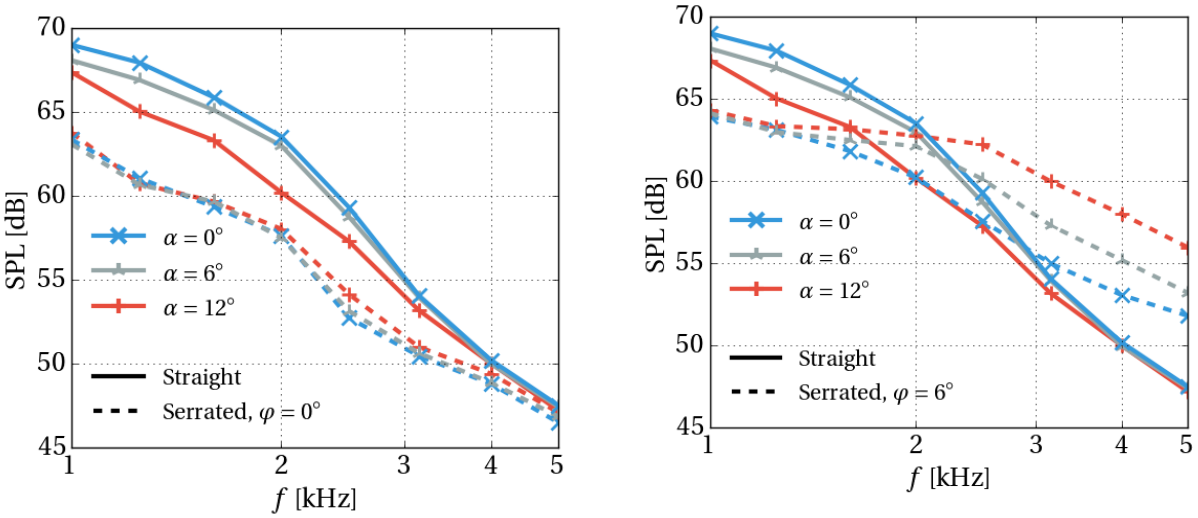


Figure 9: Third-octave band SPL for the straight and serrated trailing edges for various $\alpha$. $U_\infty = 35$ m/s, $\varphi = 0°$ (left) and $\varphi = 6°$ (right).

velocity was limited to 20 m/s.

In all cases, the LaVision software DaVis 8 was used for acquisition and processing. Multi-pass stereoscopic cross-correlation was applied, resulting in a final window size of $16 \times 16$ px overlapped by 75% (50% in the case of the 2C-PIV). For the S-PIV, a spatial resolution of 0.8 mm and vector spacing of 0.2 mm were obtained, while for the 2C-PIV it was respectively 0.24 mm and 0.12 mm. An error analysis of the measurements is omitted for conciseness and the reader is referred to Arce León et al., 2016a for further details. The random error is found to be approximately 1% in the freestream velocity and around 3% in the inner boundary layer. Considering the 2000 acquired images, the resulting error in the mean velocity is within 0.05%, and 2% for the root-mean-square (rms).

# 3. Results

## 3.1 Acoustic Emissions and Strouhal Number Evaluation

The third-octave band spectra of the trailing edge radiated sound of the straight and serrated trailing edges are shown in figure 9, for $U_\infty = 35$ m/s, at the different investigated angles of attack. The case of $\varphi = 0°$ is shown on the left, and $\varphi = 6°$ on the right.

The noise reduction capability of the serrations is evident. For $\varphi = 0°$ serrations perform reasonably well for all investigated angles of attack, reducing noise in the investigated frequency range by up to 7 dB. The application of a flap angle, $\varphi = 6°$, severely degrades their performance.

The level of noise reduction is weaker when a flap angle is present, or equivalently, the serrations appear to become a source of noise themselves beyond a certain frequency, as indicated in Gruber, Joseph, and Chong, 2011.

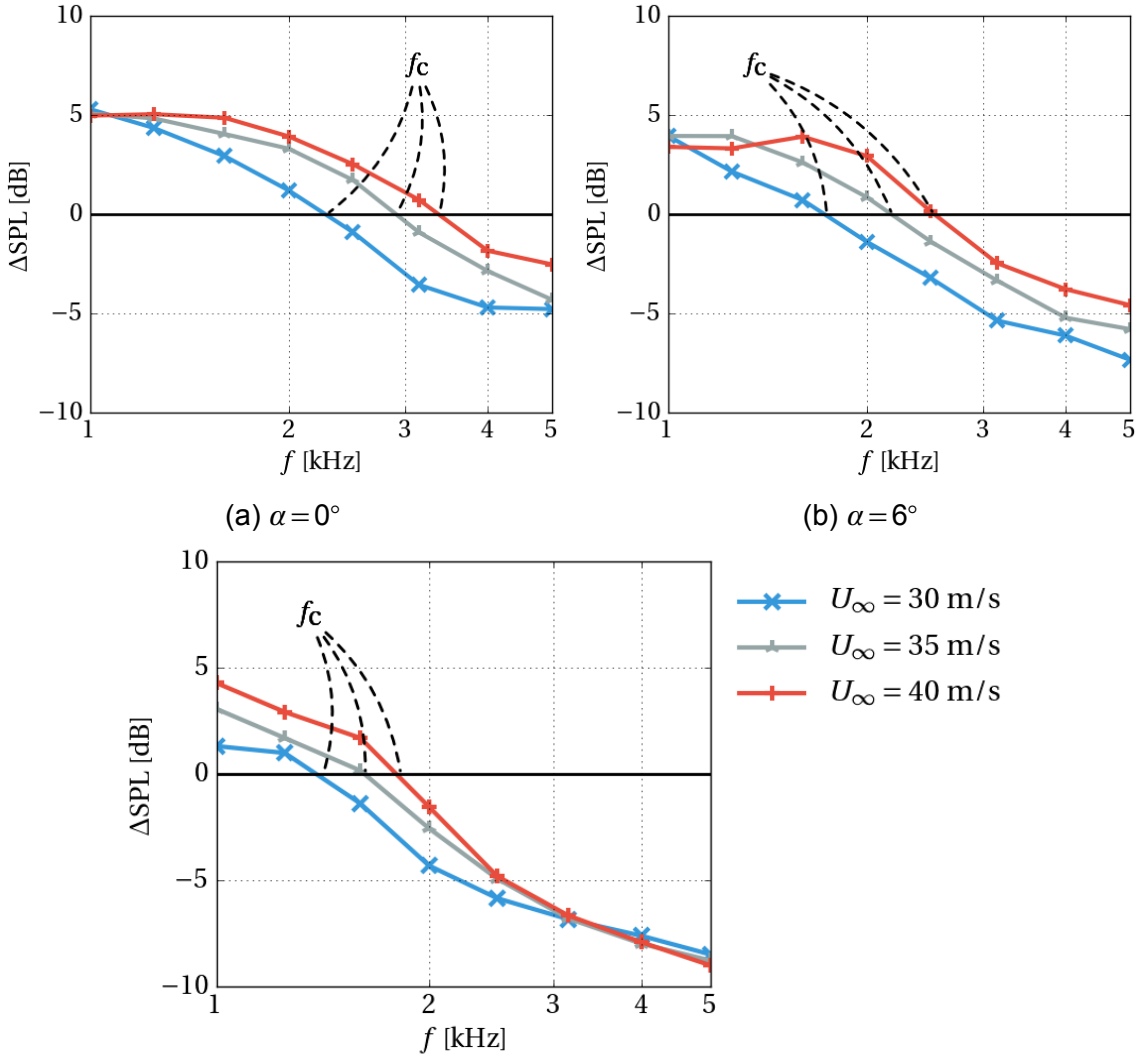


Figure 10: Noise reduction for the serrated trailing edge relative to the baseline airfoil for different $\alpha$ values and $\varphi = 6°$. The crossover frequency $f_c$ is indicated for each $U_\infty$.

To facilitate the analysis, third-octave spectra relative to the noise emissions of the straight trailing edge are presented in figure 10. Here, a positive value indicates noise reduction. The three freestream velocities are shown, at the three angles of attack, for $\varphi = 6°$. The crossover frequency, $f_c$, is indicated.

The results provide further proof that serration-flow misalignment leads to the production of noise after a certain frequency. Focus will now be paid to whether this frequency can be established using a constant Strouhal number, as suggested by Gruber, Joseph, and Chong, 2011.

The results of the calculated Strouhal number, $St_c$, for $\varphi = 6°$ are shown in figures 11 and 12. Here $f_c$ is obtained from the results shown in figure 10, and the boundary layer thickness parameters are retrieved from the measured boundary layers of the straight

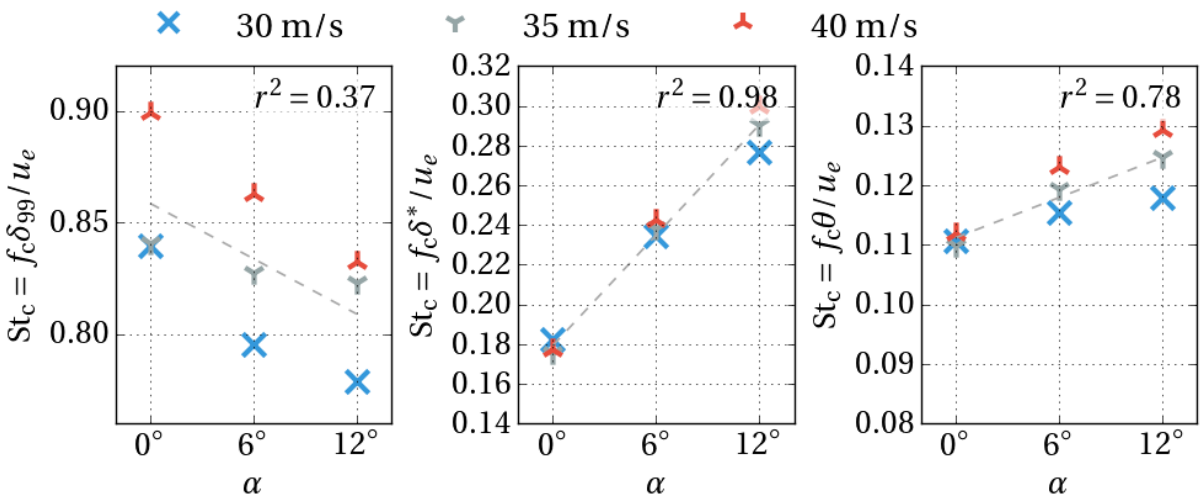


Figure 11: $\mathrm{St_c}$ for different boundary layer thickness parameters measured on the suction side. $U_\infty = 30$ m/s: ×, $U_\infty = 35$ m/s: ᛉ, $U_\infty = 40$ m/s: ⅄.

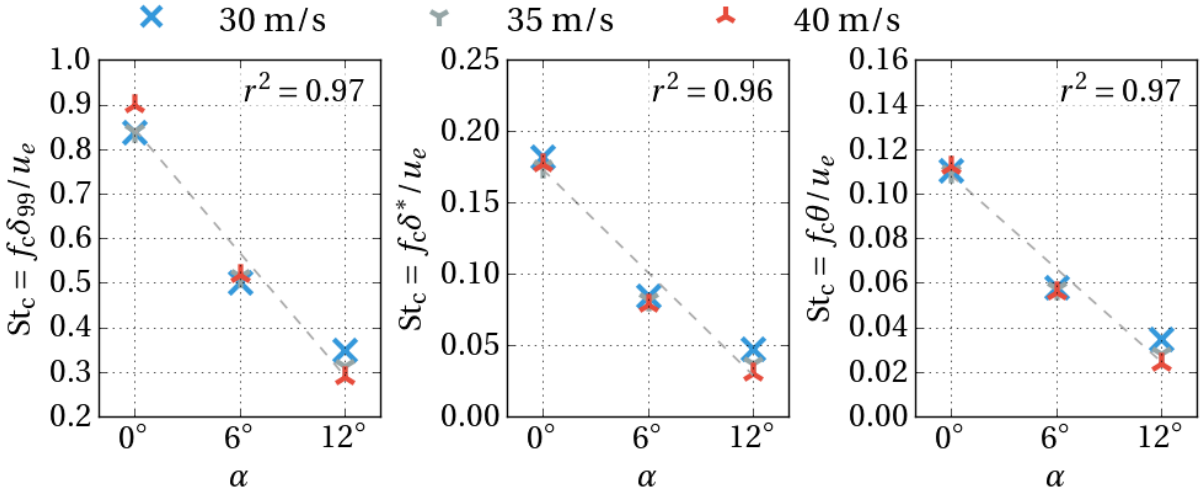


Figure 12: $\mathrm{St_c}$ for different boundary layer thickness parameters measured on the pressure side. $U_\infty = 30$ m/s: ×, $U_\infty = 35$ m/s: ᛉ, $U_\infty = 40$ m/s: ⅄.

edge. Three thickness parameters are investigated in order to verify the trend behavior of each: the $y$ location of the 99% edge velocity, $\delta_{99}$, the displacement thickness, $\delta^*$, and the momentum thickness, $\theta$. The edge velocity, $u_e$, is taken as the velocity measure for $St_c$. The results are presented for both the suction (figure 11) and the pressure sides (figure 12).

While Gruber, Joseph, and Chong, 2011 suggests that a constant Strouhal number that defines $f_c$ can be established, this is not evident from the present results. Although $St_c$ exhibits certain level of constancy across different freestream velocities for the same angle of attack, there is a general tendency for it to vary linearly for different values of $\alpha$.

In the plots, the coefficient of determination, $r^2$, is indicated. It serves to quantify the quality of a linear fit over the different values of $St_c$ for the various freestream velocities and angles of attack. It also helps to evaluate which boundary layer parameter, and which boundary layer side (pressure or suction side) would serve to better establish the behavior of $St_c$. Based on this criterion, the pressure side boundary layer thickness values appear to offer a more robust trend behavior, with higher overall values of $r^2$.

Despite not finding a universal Strouhal number related to the crossover frequency, the observed linear behavior over the different angles of attack, and its moderate uniformity over different freestream velocities indicate that $f_c$ is indeed related to the boundary layer thickness and $u_e$.

Nevertheless, developing a more general model to evaluate $f_c(St_c)$ is unlikely to be possible based on the available information. The exhibited trends are presumably dependent on the airfoil shape, and serration flap angle, variations of which are not thoroughly investigated here.

The results do however serve to suggest that the hydrodynamic source causing the increase in noise may reside on the pressure side of the serrations. This assertion is investigated in the following section.

### 3.2 Near-Edge Flow

Several features of the boundary layer flow are investigated. Focus is laid on the near-edge flow over the straight trailing edge, and over the serrated edge at $z/\lambda = 0.25$ (see figure 8). Comparisons are made between the latter at $\alpha = 12°$, and the former at $\alpha = 0°, \varphi = 0°$ and $\alpha = 12°, \varphi = 6°$. Where omitted, $\delta$ refers to $\delta_{99}$.

As indicated earlier, the measurements are taken at 20 m/s freestream velocity. This is the highest velocity at which time-resolved data can be extracted given the hardware limitations of the S-PIV system. On the other hand, at this velocity, the TBL-TE noise is too weak to allow an accurate acoustic measurement in this tunnel, and results therefore in a low SNR, with respect to the background noise. The disparity between the flow and acoustic measurement velocities will be consolidated later.

The mean flow values of the three flow components are shown in figures 13 (stream-

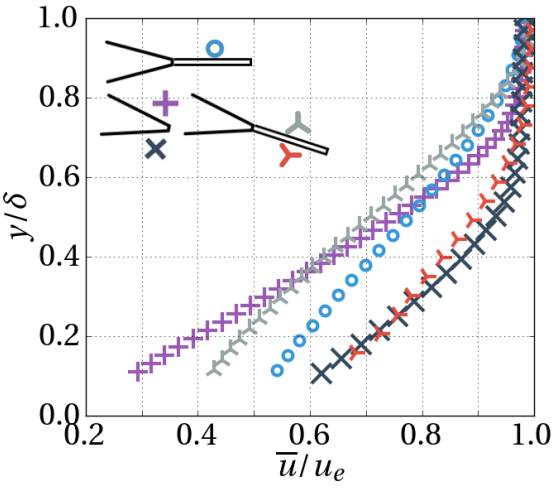


Figure 13: Streamwise mean flow component, $\overline{u}$.

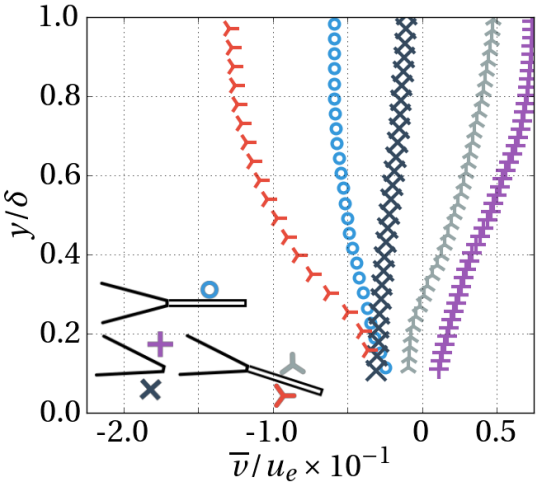


Figure 14: Wall-normal mean flow component, $\overline{v}$.

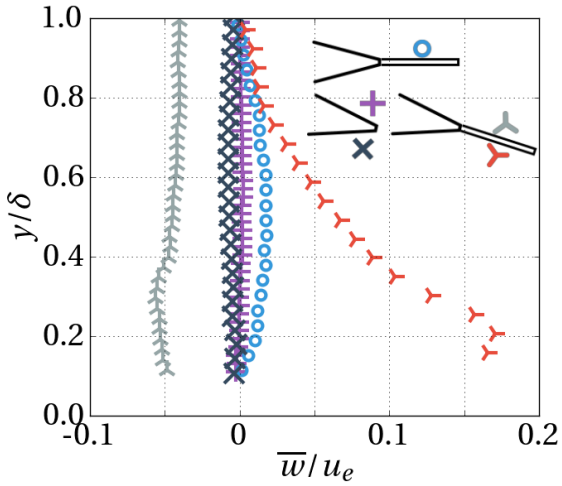


Figure 15: Spanwise mean flow component, $\overline{w}$.

wise, $\overline{u}$), 14 (wall-normal, $\overline{v}$), and 15 (spanwise, $\overline{w}$).

Noticeably higher values of $\overline{u}$ are present at the pressure side of both the straight and serrated edges at $\alpha = 12°$. On the suction side, lower values are observed with regard to the $\alpha = 0°, \varphi = 0°$ case, indicative of a higher adverse pressure gradient near the edge.

The mean wall-normal velocity component for the $\alpha = 12°, \varphi = 6°$ serrated edge configuration shows flow with an orientation towards the surface (negative values), as would be expected due to the serration misalignment. It further exhibits the largest wall-normal component magnitude between the investigated configurations. Along the suction side, the flow is oriented away from the wall, for both the serrated and straight edge cases, as expected.

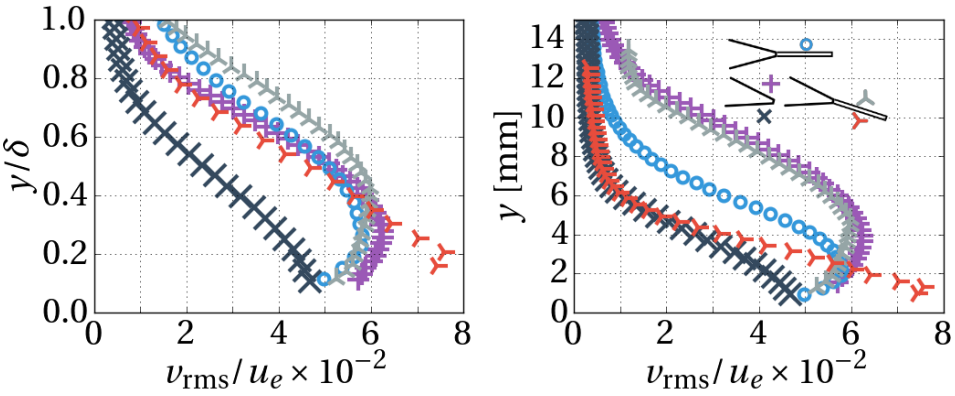


Figure 16: Wall-normal fluctuations, $v_{\text{rms}}$.

A very notable feature in the mean spanwise flow component, $\overline{w}$, is found on the pressure side of the serrated $\alpha = 12°, \varphi = 6°$ case, (figure 15). This large deviation from the other cases is a reflection of the significant spanwise flow deflection found on the pressure side in serration-flow misaligned situations, as detailed in Arce et al., 2015; Arce León et al., 2016b. The negative values observed over the suction side of the same case also relate to this condition, as flow becomes slightly deflected towards the center of the serration.

This feature correlates with a high rms observed in the $v$ component, as shown in figure 16. Here both the $\delta$-normalized (left) and absolute (right) distances from the wall are indicated. The closeness of the high $v_{\text{rms}}$ value region to the surface and the edge is evident, at about 1 mm, sustaining the assumption that it could play a role in increasing acoustic emissions. It is important to note that this feature is not present in the non-serrated airfoil, committing it to the effect that the serration misalignment has on the flow.

The measurements of $10\log_{10}\Phi_{vv}$, for $\Phi_{vv}$ the wall-normal flow component spectra, are presented in figure 17. The serrated $\alpha = 0°, \varphi = 0°$ case is omitted for brevity, but all the other cases of the previous figures are shown. The results are given for four wall-normal locations. The closest (at $y = 1.5$ mm) relates to the location of high $v_{\text{rms}}$ seen in figure 16 for the serrated case, and the furthest (12 mm) is near the edge of the boundary layer of the suction side flow. The Kolmogorov law (dashed line) is shown for reference.

The most distinct feature related to the topic investigated here is the higher turbulent energy observed beyond a frequency of about 1.1 kHz for the pressure side serrated case. The energy increases with increasing frequency, reaching over 5 dB at around 5 kHz. Its relation to the high frequency noise increase is likely, but in order to consolidate this argument, the velocity difference between the flow and acoustic measurements must first be conciliated. In order to do this, the Strouhal number relation discussed in section 2.1 is reintroduced here.

Using the observations relating to figure 12, the expected value of the acous-

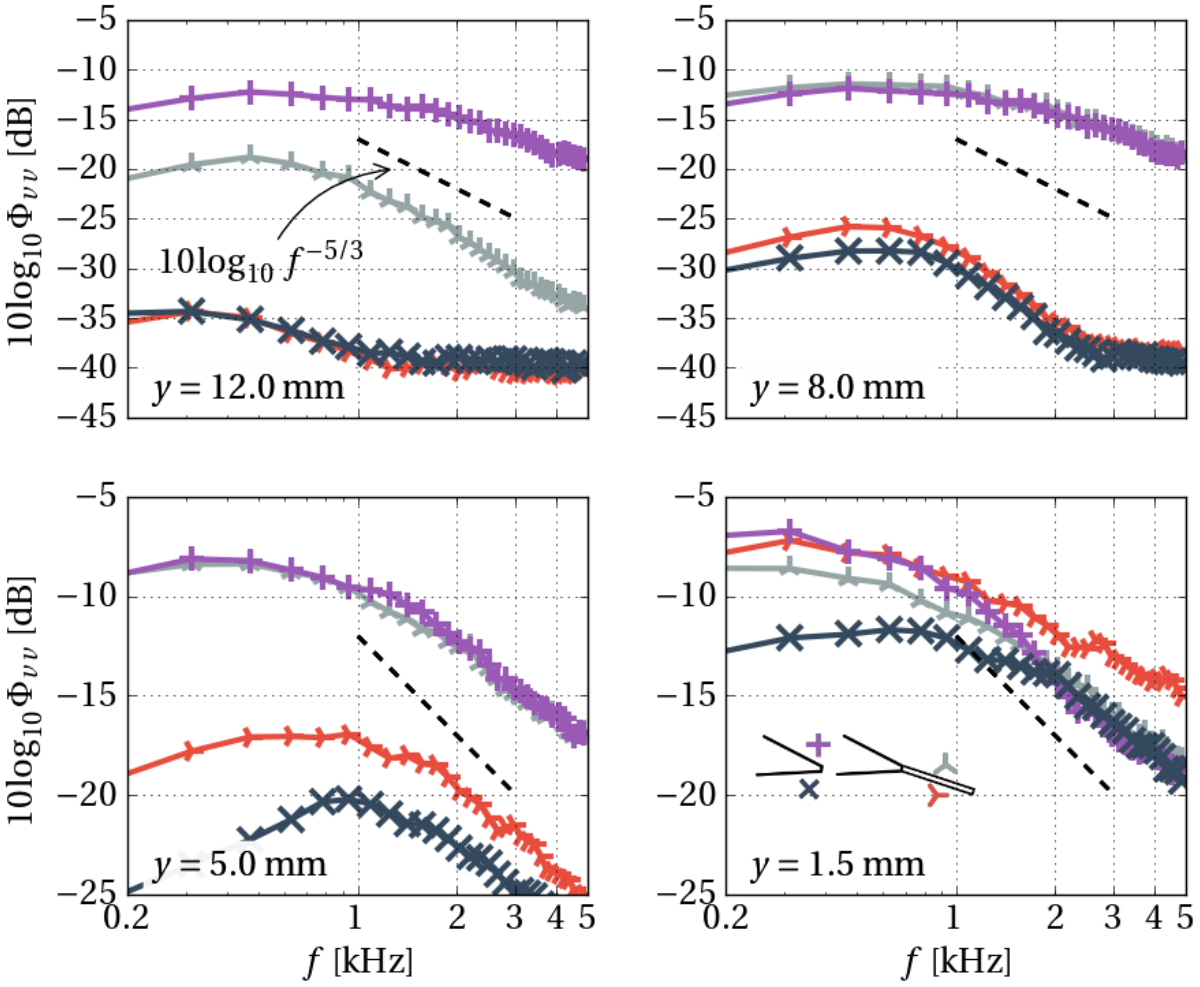


Figure 17: Spectrum of the wall-normal velocity component for different wall-normal locations.

tic crossover frequency, $f_c$, can be established for comparison with the turbulence crossover frequency at 20 m/s. This analysis is represented in figure 18.

The crossover frequency at 20 m/s is here estimated using the Strouhal numbers found above in figure 12. That is,

$$f_c = \mathrm{St}_c u_e / \delta \tag{2}$$

for $u_e = 20$ m/s and $\delta$ measured with 2C-PIV. The results using the $\mathrm{St}_c$ values found for the freestream velocities 30, 35 and 40 m/s are indicated by the symbols $\times$, $\curlyvee$ and $\curlywedge$ respectively. Since there was no perfect collapse of $\mathrm{St}_c$ found for these freestream velocities, the result of $\mathrm{St}_c$ for 20 m/s is linearly extrapolated ($+$ symbol) and used to establish $f_c$.

While the values differ depending on the boundary layer thickness parameter that is used, the results collapse to around 1.1 kHz. The mean is indicated in the figure. A correlation is then hereby established between the acoustic and turbulence crossovers.

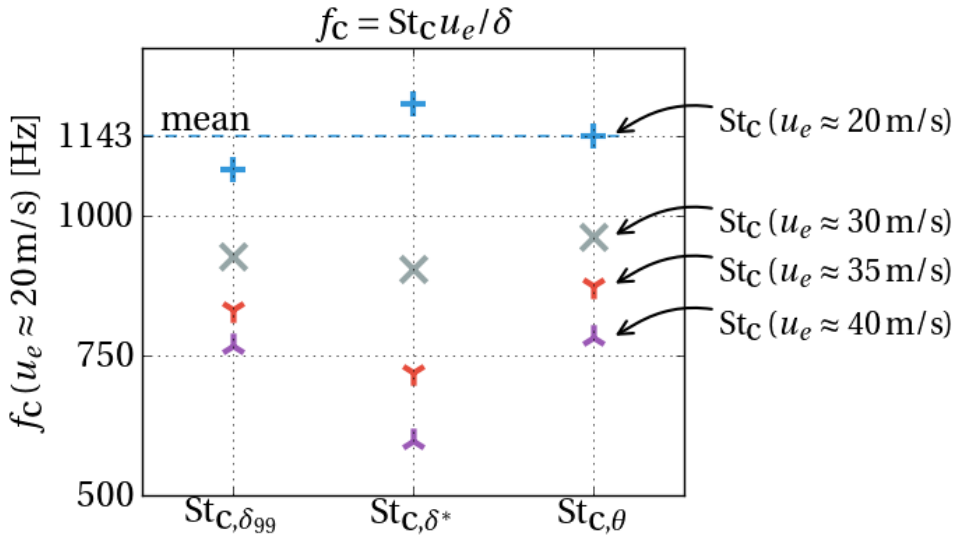


Figure 18: Predicted value of $f_c$ based on the pressure side measurements of $\mathrm{St}_c$ based on $U_\infty = 30$ m/s (×), $U_\infty = 35$ m/s (ϒ), $U_\infty = 40$ m/s (Ʌ), and the linear extrapolation to $U_\infty = 20$ m/s (+).

## 4. Conclusions

The effects of serration-flow misalignment have been investigated based on its modification of the acoustic emissions and boundary layer flow.

Measurements using acoustic beamforming confirm that an increase in noise is experienced after a certain crossover frequency, and that it is related to serration-flow misalignment.

Based on the pressure side boundary layer thickness and its edge velocity, this crossover frequency has been found to follow a linear Strouhal number behavior dependent on the angle of attack of the airfoil. While somewhat consistent Strouhal numbers were found for varying edge velocities, the idea that a single Strouhal number can be used to establish the crossover frequency is disputed, and it is more likely to be heavily dependent on angle of attack, serration flap angles, airfoil shape, and a number of other omitted parameters.

Flow measurements of the boundary layer indicate the presence of some notable features on the pressure side. A high sideways flow deflection indicated by $\overline{w}$, and a high level of $v_{\mathrm{rms}}$ that correlates to it, occur very near the surface and edge of the serration pressure side. At this location, an increase in the higher frequency turbulence energy is also observed.

The Strouhal number analysis is used to establish a relationship between this increase in the turbulence energy and that of the acoustic emissions. The crossover frequency correlation found between the two, in addition to the mean flow observations, establish that the increased source of noise is of a hydrodynamic nature, and occurs on the pressure side of flow-misaligned serrations.

## References


Arce, Carlos et al. (2015). “Flow Field Around a Serrated Trailing Edge at Incidence”. In: *33rd Wind Energy Symposium*. Kissimmee, Florida: American Institute of Aeronautics and Astronautics. ISBN: 978-1-62410-344-5. DOI: 10.2514/6.2015-0991.

Arce León, Carlos et al. (2016a). “Boundary layer characterization and acoustic measurements of flow-aligned trailing edge serrations”. In: *Experiments in Fluids* 57.12, p. 182. ISSN: 0723-4864. DOI: 10.1007/s00348-016-2272-z.

Arce León, Carlos et al. (2016b). “Flow topology and acoustic emissions of trailing edge serrations at incidence”. In: *Experiments in Fluids* 57.5, p. 91. ISSN: 0723-4864. DOI: 10.1007/s00348-016-2181-1.

Arce León, Carlos et al. (2016c). “PIV Investigation of the Flow Past Solid and Slitted Sawtooth Serrated Trailing Edges”. In: *54th AIAA Aerospace Sciences Meeting*. January. San Diego, California: American Institute of Aeronautics and Astronautics, pp. 1–15. ISBN: 978-1-62410-393-3. DOI: 10.2514/6.2016-1014.

Arce León, Carlos et al. (2017). “Effect of trailing edge serration-flow misalignment on airfoil noise emissions”. In: *Journal of Sound and Vibration* In review.

Dassen, T et al. (1996). *Results of a wind tunnel study on the reduction of airfoil self-noise by the application of serrated blade trailing edges*. Tech. rep. National Aerospace Laboratory, NLR.

Finez, A et al. (2011). “Broadband Noise Reduction of a Linear Cascade With Trailing Edge Serrations”. In: *17th AIAA/CEAS Aeroacoustics Conference (32nd AIAA Aeroacoustics Conference)*. Portland, Oregon, USA. DOI: 10.2514/6.2011-2874.

Ghaemi, Sina, Daniele Ragni, and Fulvio Scarano (2012). “PIV-based pressure fluctuations in the turbulent boundary layer”. In: *Experiments in Fluids* 53.6, pp. 1823–1840. ISSN: 0723-4864. DOI: 10.1007/s00348-012-1391-4.

Gruber, M (2012). “Airfoil noise reduction by edge treatments”. PhD thesis. University of Southampton.

Gruber, M, P Joseph, and TP Chong (2010). “Experimental investigation of airfoil self noise and turbulent wake reduction by the use of trailing edge serrations”. In: *16th AIAA/CEAS Aeroacoustics Conference*, pp. 1–23.

Gruber, Mathieu, Phillip Joseph, and Tze Chong (2011). “On the mechanisms of serrated airfoil trailing edge noise reduction”. In: *17th AIAA/CEAS Aeroacoustics Conference (32nd AIAA Aeroacoustics Conference)*. Vol. 2781. June. Portland, Oregon, USA: American Institute of Aeronautics and Astronautics, pp. 5–8. ISBN: 978-1-60086-943-3. DOI: 10.2514/6.2011-2781.

Hurault, J et al. (2015). “Aeroacoustic wind tunnel experiment for serration design optimisation and its application to a wind turbine rotor”. In: *6th International Meeting on Wind Turbine Noise*. Glasgow.

Johnson, Don H. and Dan E. Dudgeon (1993). *Array Signal Processing, Concepts and Techniques*. ISBN: 9780130485137. P T R Prentice Hall, Englewood Cliffs.

Mathew, J et al. (2016). “Serration Design Methodology for Wind Turbine Noise Reduction”. In: *Journal of Physics: Conference Series* 753, p. 022019. ISSN: 1742-6588. DOI: 10.1088/1742-6596/753/2/022019.

Mueller, TJ (2002). *Aeroacoustic Measurements*. ISBN-978-3-642-07514-8. Springer Science & Business Media, p. 313. ISBN: 3540417575.

Oerlemans, S et al. (2009). “Reduction of wind turbine noise using optimized airfoils and trailing-edge serrations”. In: *AIAA Journal* 47.6, pp. 1470–1481. ISSN: 0001-1452. DOI: 10.2514/1.38888.

Oerlemans, Stefan (2016). “Reduction of wind turbine noise using blade trailing edge devices”. In: *22nd AIAA/CEAS Aeroacoustics Conference*, pp. 1–18. DOI: 10.2514/6.2016-3018.

Pröbsting, S. et al. (2016). “Vortex shedding noise from a beveled trailing edge”. In: *International Journal of Aeroacoustics* 15.8, pp. 712–733. ISSN: 1475-472X. DOI: 10.1177/1475472X16666633.

Sijtsma, P. (2010). *Phased array beamforming applied to wind tunnel and fly-over tests*. Tech. rep. NLR-TP-2010-549. Anthony Fokkerweg 2, 1059 CM Amsterdam, P.O. Box 90502, 1006 BM Amsterdam, The Netherlands: National Aerospace Laboratory (NLR).

Vathylakis, Alexandros, Tze Pei Chong, and Phillip F. Joseph (2015). “Poro-Serrated Trailing-Edge Devices for Airfoil Self-Noise Reduction”. In: *AIAA Journal*, pp. 1–16. ISSN: 0001-1452. DOI: 10.2514/1.J053983.

Vathylakis, Alexandros et al. (2016). “Sensitivity of aerofoil self-noise reductions to serration flap angles”. In: *22nd AIAA/CEAS Aeroacoustics Conference*, pp. 1–17. DOI: 10.2514/6.2016-2837.